



Article

Cite this article: Homma T, Hirai K, Kumiko GA, Azuma N (2025) Dislocation density measurements in crept artificial ice with and without microparticles using modified Williamson-Hall and Warren-Averbach methods. *Journal of Glaciology* **71**, e34, 1–10. <https://doi.org/10.1017/jog.2025.4>

Received: 22 February 2024

Revised: 22 December 2024

Accepted: 8 January 2025

Keywords:

artificial ice; creep; dislocation density; ice sheet; microparticle; X-ray diffraction

Corresponding author: Tomoyuki Homma;
Email: thomma@mech.nagaokaut.ac.jp

Dislocation density measurements in crept artificial ice with and without microparticles using modified Williamson-Hall and Warren-Averbach methods

Tomoyuki Homma¹ , Kazuteru Hirai¹, Goto-Azuma Kumiko²  and Nobuhiko Azuma¹

¹Department of Mechanical Engineering, Nagaoka University of Technology, Nagaoka, Japan and ²National Institute of Polar Research, Research Organization of Information and Systems, Tokyo, Japan

Abstract

To investigate dislocation densities of deformed polycrystalline ice the modified Warren-Averbach and modified Williamson-Hall plots of X-ray line broadening have been applied to artificial ice with and without silica particles, which model microparticles in ice sheets. This also provides us with the dislocation velocity during creep. Creep tests were conducted at -20°C and 2 MPa by altering the strains using the artificial ice. In the primary creep region the ice with microparticles is remarkably deformed, and the strain rate is suppressed because of high dislocation densities. At 10% strain the dislocation density shows the maximum value due to the continuous dislocation pile-ups in the silica-containing ice: the dislocation density in the pure ice remains almost constant within the maximum strain used in this study. As the strains continuously decrease, microparticles pin the grain boundaries, leading to small grain sizes. Such small grain sizes provide sinks for dislocation annihilations, resulting in decrease in the dislocation densities in the silica-containing ice.

1. Introduction

The global mean sea level has risen faster with acceleration in recent decades. It has been reported that the sea-level changes occur due to ice loss particularly in the Greenland ice sheet. However, it has also been reported that the acceleration in mass loss between 2006 and 2015 was at an average rate of $278 \pm 11 \text{ Gt yr}^{-1}$ from Greenland and $155 \pm 19 \text{ Gt yr}^{-1}$ from Antarctica (IPCC, 2019: Summary for Policymakers). One of the reasons for mass loss is believed to be related to the ice sheet flows from Greenland and Antarctica. As mentioned above the ice sheet mass loss is particularly significant in Greenland. Such flows can occur due to basal slip on the soil surface and deformation of ice (Cuffey and Paterson, 2010). The latter is related to the creep phenomenon with the assistance of dislocation motions under applied stress and temperature. The concept of creep of ice is well established for natural ice sheets and experimental artificial ice, although it is known that a universal constitutive law for ice does not exist. For example well-known Glen's flow law explains how ice plastically deforms (Glen, 1955). During creep deformation particularly in a tertiary creep regime dynamic recrystallisation usually takes place (Duval, 1981; Duval and others, 1983) with fabric development. Budd and Jacka (Budd and Jacka, 1989) summarised different creep behaviours between ice sheets and artificial ice due to different stress fields and crystal orientations. Although anisotropic ice deformation was common in the ice sheet, it was ill-considered in the flow-law model. Azuma investigated the deformation behaviours of anisotropic polycrystalline ice and then constructed a power-law creep equation with a steady-state creep rate, including the mean Schmid factor in the pre-exponential factor (Azuma, 1995), and then extended it to the Cartesian coordinate system (Azuma, 1994; Azuma and Goto-Azuma, 1996).

One of the important factors affecting deformation behaviour in ice is the existence of microparticles. The reasons for the presence of such impurities in ice could be related to minerals of continental origins, sea salts, biological origins and so on. In an earlier study ultrafine amorphous silica was artificially dispersed in ice (Nayar and others, 1971). To model the base of an ice sheet which usually includes a layer of dirty ice several meters in thickness, sand was included in artificial ice (Hooke and others, 1972). These creep experiments show strengthening effects due to the existence of sands in ice on creep deformation. On the other hand the presence of particles in ice also affects dynamic recrystallisation or grain boundary migration during creep (Humphreys and Hathery, 2004), depending on the stress level (Song and others, 2004, 2008), resulting in softening of the ice. This discrepancy between the effects of particles on hardening or softening of creep deformation of ice

© The Author(s), 2025. Published by Cambridge University Press on behalf of International Glaciological Society. This is an Open Access article, distributed under the terms of the Creative Commons Attribution licence (<http://creativecommons.org/licenses/by/4.0>), which permits unrestricted re-use, distribution and reproduction, provided the original article is properly cited.

cambridge.org/jog



Table 1. Experimental conditions of creep deformation using artificial ice

Type	Impurities	Impurity content	Impurity diameter	Applied stress MPa	Test temperature °C	Sample diameter cm	Sample height or gauge length cm	Grain diameter of ice	References
Tension	ultrafine amorphous silica	0.5 or 1 vol. %	150 Å	0.5 ~ 1.8	-22 ~ -2	1.3	5.7	0.25 ~ 0.5 mm 4 – 8 cm long	Nayar and others, 1971
Compression	sand	0.013 ~ 0.347 vol. %	64 mm	0.53 ~ 0.64	-9.2 ~ -7.4	1.95	10	300 ~ 500 mm	Hooke and others, 1972
Compression	silt	0.1 ~ 4 mass %	0.05 mm	1.45	-12	5.0	12.7	3 ~ 5 mm	Song and others, 2004
Compression	silt	0.43 vol. %	50 mm	0.4 ~ 1.45	-10 ~ -5	5.0	12.7	5 mm	Song and others, 2008
Compression	silica	0.01 or 0.1 mass%	0.3 mm	0.2 ~ 1.0	-50 ~ -5	1.5	3	30 ~ 107 μm	Saruya and others, 2019

could be related to the average grain size of the ice and particles. We then tested making a fine-grained ice with a few tens of micrometres in diameter, containing micro- particles with 300 nm in diameter and found that the addition of microparticle softens the ice during creep, and the corresponding strain rate-strain curves do not show clear appearance of a steady state, irrespective of the microparticle additions. Thus, it is concluded that the recovery of dislocation pile-ups due to lattice diffusion based on a dislocation creep mechanism is the rate-controlling process, and the microparticles insignificantly influence the deformation of the fine-grained ice, except for their effect on grain boundary pinning (Saruya and others, 2019). The details of the creep conditions mentioned above are given in Table 1.

When considering a dislocation glide or climb during creep deformation, the creep rate $\dot{\epsilon}$ in both cases can be described by the well-known Orowan equation,

$$\dot{\epsilon} = \rho b v \quad (1)$$

where ρ is dislocation density, b the Burgers vector and v the average velocity of dislocations (Poirier, 1976; Cuffey and Paterson, 2010). In the case of steady-state creep under a constant-stress condition the steady-state creep rate is expressed as $\dot{\epsilon} \propto \sigma^m$, according to Weertman (Weertman, 1973). Here m is a stress exponent. More details will be discussed later. Based on these equations we understand that the dislocation density is one of the important factors in determining the steady-state creep rate. The parameters used in equations are shown in Table 2.

First systematic deformation experiments of water-frozen ‘single-crystal’ ice were conducted by Glen (Glen, 1952). He observed that slips appear after a tensile test. Nakaya was the first to report plastic deformation behaviours in single crystalline ice from the Mendenhall Glacier in Alaska with the aid of dislocations, showing slip lines during a bending test, which were observed by Foucault’s method of shadow photography (Nakaya, 1956). He then found that gliding planes appeared after bending the single crystalline ice. He attributed this to the occurrence of slips related to the dislocations. In the early stage of the research the existence of dislocations was *indirectly* confirmed using an etch-pit method and electron microscopy for lake ice (Muguruma, 1961). However the observations of the dislocations in ice were successfully made using X-ray photographs (X-ray diffraction topography) as reported by Hayer and Webb (Hayes and Webb, 1965) and were then extensively analysed by Higashi *et al.* using the X-ray diffraction topography (Fukuda and Higashi, 1969; Higashi,

Table 2. Symbols and definitions in equations

Symbol	Definition	Symbol	Definition
$\dot{\epsilon}$	creep rate	ΔK	$2\cos\theta (\Delta\theta) / \lambda$
ρ	dislocation density	$\Delta\theta$	measured Bragg angles of line profile
b	Burgers vector	D	volume averaged grain size
v	average dislocation velocity	H	constant
A_n	Fourier series	\bar{C}	average dislocation contrast factor
n	an index ranging from $-\infty$ to ∞ including zero	H'	constant
A_n^p	particle size coefficient of Fourier series	U	correlation factor
A_n^D	distortion coefficient of Fourier series	$\bar{C}_{hk.l}$	average dislocation contrast factor
hkl	Miller index	q_1, q_2	fitting parameters
δ	spectral integral line breadth	x	$(2/3)(c/a)^2$
λ	X-ray wavelength	a	lattice parameter of hexagonal material
t	mean linear dimension of grain	c	lattice parameter of hexagonal material
θ	Bragg angle	α	$0.9/D$
ξ	strain distribution	κ	$(H^2 b^2 / 2)^{1/2} \rho^{1/2}$
I_g	diffracted intensity	L	Fourier length
A_g	Fourier transform of I_g	θ_1, θ_2	measured Bragg angles of line profile
θ_0	Bragg angle of undistorted lattice	R_1, R_2	auxiliary constants
g	reciprocal lattice vector	B	constant
ϵ_n	strain	σ	applied stress
W	elastic strain energy of dislocations per unit length	m	stress exponent
C	dislocation contrast factor	Q	activation energy
μ	shear modulus	k	Boltzmann’s constant
R_e	outer cutoff radius of dislocation	T	absolute temperature
r_0	inner cutoff radius of dislocation	β	constant
E	Young’s modulus	γ	constant
K	$\sin\theta / \lambda$		

1988) based on the Lang method (Lang, 1959). Nevertheless, while the X-ray diffraction topography was a powerful tool to *directly* reveal dislocations in the single crystals, the measurable dislocation densities were limited to around 10^2 cm^{-2} (10^6 m^{-2}). Instead of measuring dislocation densities by X-ray diffraction topography Hori et al. applied an X-ray diffraction method to obtain dislocation densities in the Vostok ice core from the rocking-curve measurements with Cu-K α radiations (Hori and others, 2004). The instrument was installed in a cold room kept at -20°C , and a (10 $\bar{1}$ 2) reflection in each crystal was analysed. It was found that the measured dislocation densities ranged from 1.9×10^8 to $2.4 \times 10^{10} \text{ m}^{-2}$, and large numbers of dislocations were detected in the glacier ice extracted from a depth of around 3286 m.

The measurements of dislocation densities were significantly developed by Krivoglaz and Wilkens and Ungár (Krivoglaz, 1969; Wilkens, 1969; Ungár and others, 1998). It is well known that both contributions from grain sizes of the matrix of polycrystalline materials and strains are involved in the diffracted-peak intensities. As described by Hori and others (Hori and others, 2004), they only chose the (10 $\bar{1}$ 2) reflections for the diffracted intensities of the ice cores. In their appendix, they considered the effect of the dot product of \mathbf{g} and \mathbf{b} , where \mathbf{g} and \mathbf{b} are reciprocal lattice and Burgers vectors, respectively, in order to have contrast. Krivoglaz and Wilkens included the dislocation contrast factor as an effect of the strains, which will be discussed in more detail in the experimental methods section of this paper. This method, known as the *modified Warren-Averbach* and *modified Williamson-Hall* plots, can obtain more precise dislocation densities in strained materials, even in deformed ice. Nevertheless, such an approach has never been applied to ice.

In order to evaluate the dislocation densities in deformed ice samples using the modified Warren-Averbach and modified Williamson-Hall plots of X-ray line broadening we developed an apparatus that to be located inside a commercial XRD instrument with Cu-K α radiations to maintain ice at low temperatures. By using this method we succeeded in accurately measuring the dislocation densities in ice as a function of the creep strain at -20°C under an applied stress of 2 MPa. The effect of microparticles on the dislocation densities is also discussed.

2. Experimental methods

2.1. Sample preparations

Ultra-pure water (18.2 M Ω -cm) was sprayed into liquid nitrogen in order to produce ice powders. Additionally SiO $_2$ (silica) powders, simulating impurities in ice cores, with a diameter of 300 nm and an amorphous structure were mixed with the ice powders. Two different artificial ice samples were prepared; (1) pure ice powders and (2) pure ice powders mixed with microparticles containing ice. The latter contained 0.1 mass% silica in the ice. These powders were sieved with a mesh size of 710 μm so as to obtain a uniform powder size. The powders were loaded into a metallic die and then sintered at a cold room maintained at -10°C for 1 h and pressed at 70 MPa using a hydraulic jack. During the sintering the inside of the die was evacuated by a rotary pump to remove air bubbles as much as possible (Azuma and others, 2012). The average dimensions of the sintered ice with a diameter of 33 mm and a height of 65 mm were cut. The obtained artificial ice had polycrystalline microstructures.

Creep specimens were cut from a sintered sample into four pieces with equivalent volumes, and then each piece was turned on a lathe to shape the specimen into a cylinder with a diameter of 15 mm and a height of 30 mm.

2.2. Uniaxial compressive tests of the bulk specimens

Creep specimens were immersed in a container filled with silicone oil to prevent sublimation during the test and to suppress friction between the specimen and jig. A load was applied to the cylindrical creep specimen parallel to its long axis and controlled to maintain the applied stress at 2 MPa. The creep test machine was placed in a constant temperature bath inside a freezer maintained at -20°C . The strain was measured using the digital displacement meter (Mitutoyo ID-F125) attached to the creep machine.

2.3. Microstructural observations

The microstructures before and after the creep tests were observed using an optical microscope (Olympus BX51). The samples were cut from the cylindrical specimens used for the creep tests, and the observation directions were fixed perpendicular to the long axis of the cylindrical specimens. The upper and bottom parts of the cylinder were cut about 10 mm from the edges, and a remaining 10 mm part located near the centre of the cylinder was used. The average grain diameter was calculated based on the equivalent circle diameter after measuring the area of each grain using Image J. Additionally, subgrain boundary densities were also calculated by measuring the length of the subgrain boundaries using Image J within the area of a field of view.

2.4. Sample holder for X-ray diffraction analyses

The X-ray diffraction analyses were performed using a commercial XRD machine (Rigaku Ultima IV) installed in a room maintained at ambient temperature. A sample holder shown in Figure 1a was made of a Cu plate (thermal conductivity: $400 \text{ W m}^{-1} \text{ K}^{-1}$), with blocks of thermal insulators made of Teflon covering the top surface, except for the space parallel to the beam line. The ice was maintained between the Teflon blocks, which were 8 mm thick, on the Cu plate and cooled at -20°C . After fixing the ice sample to the Cu plate in a cold room kept at -10°C , the space was sealed using a Kapton tape with a width of 20 mm so that it did not disturb the X-ray emissions to the surface of the ice at large Bragg angles. The Cu plate was cooled using a container which was made of an A5052P aluminium alloy (thermal conductivity: $200 \text{ W m}^{-1} \text{ K}^{-1}$) and filled with cooling nitrogen gas (purity of 99.9%) flowing into a helical and 750-mm-long Cu tube kept in liquid nitrogen at -196°C as shown in Figures 1c and d. The sample holder was easily removable and placed on the cooling container just before starting the X-ray analysis. The container could be adjusted to the central position by an XYZ linier translation stage, and the optimum height was adjusted using a stereomicroscope (Figure 1b). The surface of the Kapton tape was gently covered with dry air to prevent frosting due to moisture absorption from the air in the experimental room maintained at ambient temperature. The X-ray radiation used was Cu-K α with a wavelength of 0.15406 nm. The tube voltage and current used were 40 kV and 20 mA, respectively. The step size and scan speed used were 0.01° and 0.2°

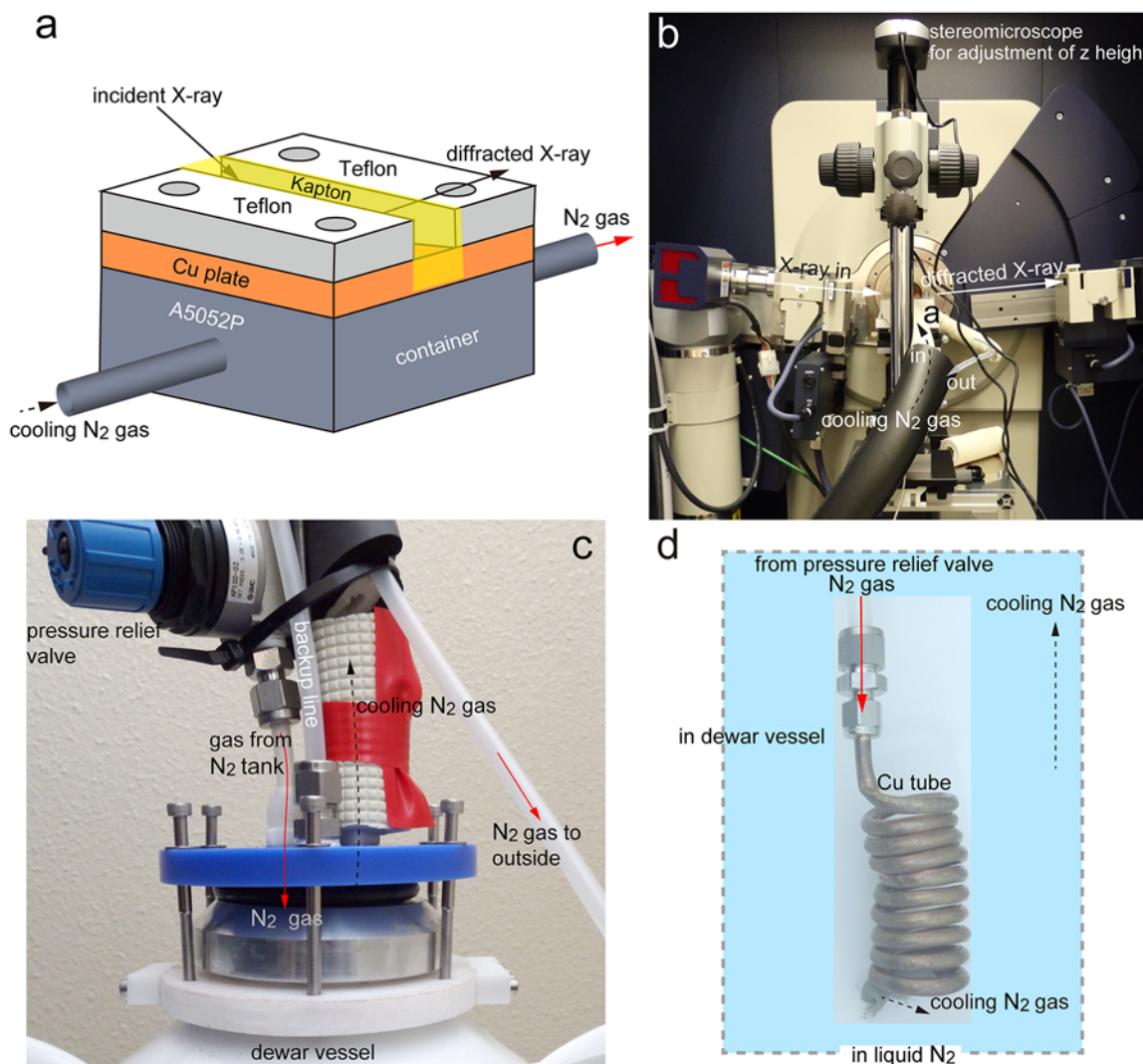


Figure 1. (a) design of removable sample holder, (b) arrangement of x-ray generator, sample holder and x-ray detector in ultima IV, (c) at the top of the dewar vessel poured liquid nitrogen and (d) a helical and 750-mm-long cu tube which was immersed in liquid nitrogen.

min^{-1} , respectively. The schematics of the developed cooling system for the X-ray measurements of ice samples are summarised in Figure 2.

2.5. Dislocation density measurements

At least two independent parameters of grain size and strain in polycrystalline materials are included in diffracted intensities of the X-ray (Warren and Averbach, 1950). The shape of a diffracted intensity can be represented by a Fourier series, and it is expressed as

$$A_n(l) = A_n^p A_n^d(l) \quad (2)$$

where n is an index ranging from $-\infty$ to ∞ including zero, l is the Miller index given e.g. by $(00l)$ and A_n^p and $A_n^d(l)$ are particle size and distortion coefficients, respectively (Warren and Averbach, 1952). Williamson and Hall originally reported the composite broadening of diffracted intensities in X-ray diffraction (XRD) produced by particle size and strain effects (Williamson and Hall,

1953), expressed by

$$\delta = \frac{\lambda}{t \cos \theta} + 2\xi \tan \theta \quad (3)$$

where δ is a spectral integral line breadth, λ the X-ray wavelength, t a mean linear dimension of the grain, θ the Bragg angle and ξ the strain distribution. If the well-known Eq. (3) is rearranged, e.g., to

$$\frac{\delta \cos \theta}{\lambda} = \frac{1}{t} + \frac{2\xi \sin \theta}{\lambda} \quad (4)$$

then from the intercept and slope of the $\delta \cos \theta / \lambda - 2 \sin \theta / \lambda$ diagram, the particle size t and strain ξ can readily be extracted. However, the scattering of the X-rays is significantly affected by the incident beam direction, dislocation direction, the Burgers vector and elastic anisotropy of the crystals. To improve the accuracy of the measurement the *dislocation contrast factor* was included in the theory of the broadening of the X-ray intensities by Krivoglaz and Wilkens (Krivoglaz, 1969; Wilkens, 1969). This was then extended to be analysed from the actual XRD patterns of cubic crystals (Groma and others, 1988; Ungár and others, 1998), and was applied

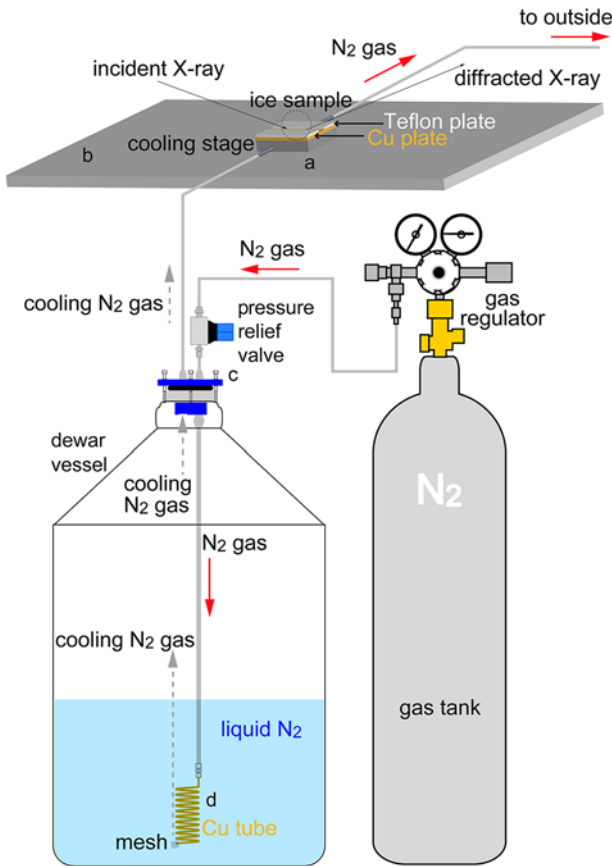


Figure 2. Schematic of the developed cooling system for x-ray measurements of ice samples using N₂ gas and liquid N₂. Symbols (a) to (d) correspond to Figures 1a to 1d, respectively.

for hexagonal crystals (Klimanek and Kužel, 1988; Ungár and others, 2001; Dragomir and Ungár, 2002).

The intuitive expression of the diffracted intensity $I_g(S)$ including the effect of elastic strains can be explained by (Wilkins, 1969)

$$I_g = \int A_g(n) \exp(2\pi i n S) dn \quad (5)$$

where $A_g(n)$ is the Fourier transform of $I_g(S)$ which is normalised to unity, $S = 2(\sin\theta - \sin\theta_0)/\lambda$, θ diffraction angle, θ_0 the Bragg angle of the undistorted lattice and λ the X-ray wavelength. The effect of strains ε_n is inserted in $A_g(n)$ as

$$A_g(n) = \langle \exp(2\pi i g n \cdot \varepsilon_n) \rangle \quad (6)$$

The brackets $\langle \rangle$ indicate a mean value and g the reciprocal lattice vector. According to the theory of dislocations the elastic strain energy of dislocations per unit length can be expressed as (Wilkins, 1967; Hirth and Lothe, 1968)

$$W = C \frac{\mu b^2}{4\pi} \rho \log\left(\frac{R_e}{r_0}\right) \quad (7)$$

where μ is the shear modulus. Additionally, Wilkins derived the following equation for the mean square of the differential strain using Eq. (7) and a rough approximation of Young's modulus

$E = 2\mu$ by considering Poisson's ratio as 0.325 (Petrenko and Whitworth, 1999),

$$\langle \varepsilon_0^2 \rangle = \frac{b^2}{4\pi} \rho C \log\left(\frac{R_e}{r_0}\right) \quad (8)$$

here C is the dislocation contrast factor, R_e and r_0 are the outer and inner cutoff radii of the dislocation, respectively. Thus we realise from Eqs. (5), (6) and (8) that the intensity profiles of XRD patterns can be broadened due to the presence of strains related to the dislocations whose effect is included in the parameter of C .

The obtained X-ray profiles were fitted using the Lorentz function. The modified Warren-Averbach (WA) and modified Williamson-Hall (WH) plots were then used to evaluate the dislocation densities as a function of the creep strain. Here we assign $K = 2\sin\theta/\lambda$ and $\Delta K = 2\cos\theta(\Delta\theta)/\lambda$. The full width at half-maximum (FWHM) of line profiles can be given as

$$\Delta K = \frac{0.9}{D} + \left(\frac{\pi H^2 b^2}{2}\right)^{1/2} \rho^{1/2} K \bar{C}^{1/2} + \left(\frac{\pi H' b^2}{2}\right) U^{1/2} K^2 \bar{C} \quad (9)$$

where D is the volume averaged grain size, H a constant, \bar{C} the average dislocation contrast factor, H' a constant and U a correlation factor (Ungár and others, 1998). The last term in Eq. (9) is usually small and hence it can be neglected. Eq. (9) is known as the modified WH plot. In the case of hexagonal materials the average dislocation contrast factors are expressed as (Dragomir and Ungár, 2002).

$$\bar{C}_{hk.l} = \bar{C}_{hk.0}(1 + q_1 x + q_2 x^2) \quad (10)$$

where q_1 and q_2 are fitting parameters and $x = (2/3)(c/a)^2$: a and c are lattice parameters of the hexagonal materials, and c is measured parallel to the c axis. From Eqs. (9) and (10)

$$\frac{(\Delta K)^2 - \alpha}{K^2} = \kappa \bar{C}_{hk.0}(1 + q_1 x + q_2 x^2) \quad (11)$$

is derived, where α is $0.9/D$ and $\kappa = (H^2 b^2/2)^{1/2} \rho^{1/2}$.

The modified WA plot is given by

$$\ln A(L) \approx \ln A^p(L) - \left(\frac{\pi \rho b^2 L^2}{2}\right) \ln\left(\frac{R_e}{L}\right) K^2 \bar{C} + \left(\frac{U \pi^2 b^4 L^4}{4}\right) \times \ln\left(\frac{R_1}{L}\right) \ln\left(\frac{R_2}{L}\right) K^4 \bar{C}^2 \quad (12)$$

where $L = na_3$ is the Fourier length, $a_3 = \lambda/2(\sin\theta_2 - \sin\theta_1)$ is in the direction of the diffraction vector g and the line profile is measured from θ_1 to θ_2 of an angular range, $A^p(L)$ is the size contribution to the Fourier coefficient for the intensity distribution and R_1 and R_2 are auxiliary constants which are not interpreted physically (Ungár and others, 1998). Eq. (12) can be simplified such as

$$\ln A(L) \approx \tau - \varphi K^2 b^2 \bar{C} + oK^4 b^4 \bar{C}^2 \quad (13)$$

and the last term is omitted and then the parameter φ becomes a fitting parameter when a $\ln A(L) - K^2 b^2 \bar{C}$ diagram is drawn by selecting several Bragg peaks in the line profile

$$\varphi = \rho \frac{\pi L^2}{2} \ln\left(\frac{R_e}{L}\right) \quad (14)$$

From Eq. (14) we can create a diagram of $\varphi/L^2 - \ln L$, and it reveals the dislocation density from the slope of $-\pi\rho/2$. The dislocation density was indeed measured as the sum of mobile and immobile dislocations using this technique.

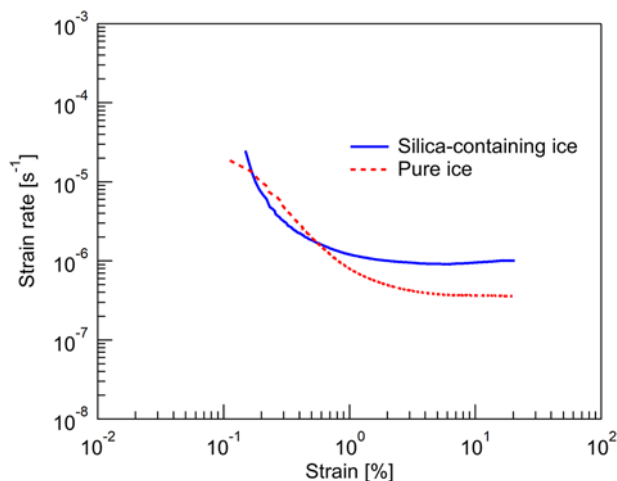


Figure 3. Strain rate and strain diagrams of pure and silica-containing ice measured at 20°C and 2 MPa after the creep tests.

3. Results and discussion

3.1. Creep curves

The measured strain rate and strain diagrams associated with the creep experiments are given in Figure 3, which show samples crept to 20% strain. Both samples show concave upward behaviours as a function of the strain: as the strain increases, the strain rate decreases. The initial trends of the strain rates are very similar to those reported earlier in our paper (Saruya and others, 2019); that is, the pure ice shows slightly concave downward behaviour up to $\approx 0.36\%$ strain, while the silica-containing ice shows a rapid decrease in the strain rate until around 0.5% strain. This means that silica may promote creep deformation particularly in the early stages of the creep deformation in the primary creep region. However pure ice shows continuous decrease in the strain rate within our experimental conditions. As a result the silica-containing ice is much softer than the pure ice above 0.56% strain. This result is consistent with that reported by Saruya and others (2019).

3.2. Microstructural observations and quantifications of grain size and subgrain boundary density

The creep tests were conducted up to 1, 10 and 20% strains in both the pure and silica-containing ice based on Figure 3. The observed microstructures are shown in Figure 4. The quantitative results associated with the average grain size and subgrain boundary density as a function of the strain are given in Figure 5. In the initial state before the creep deformations grain boundaries (GBs) indicated by black arrows are well distinguished. The shape of GBs is equiaxed and appears straight. Additionally, some spherical and weak contrasts are seen in the silica-containing ice, as indicated by white arrowheads. They are the silica particles, but they appear aggregated when observed with the optical microscope (OM).

Once stress is applied to the ice (1% strain), subgrain boundaries (sGBs) shown by white arrows appear within the grains particularly in the pure ice. They divide the crystal into several subgrains. Since there are no silica particles, dislocations can move easily. Large amounts of dislocations are generated as the 1% strain is within the primary creep regime. Thus both grain refinements and increases in sGB density occur in the pure ice as indicated

in Figure 5. However the sGBs are rarely observed in the silica-containing ice at the 1% strain. The grain size also hardly changes, due to the pinning effect of the silica particles on the GBs (Figure 5). The drastic changes in the microstructures occur in the 10% strain. In both the samples the appearances of dynamic recrystallisation are obvious, and average grain sizes decrease. SGB densities also increase; it is readily estimated that large amounts of dislocations are introduced in the samples. Both microstructures are very similar, as shown in Figure 4, and therefore the quantitative results in Figure 5 also reveal similar trends. At 20% strain apparent grain growth can be confirmed in the pure ice, as shown in Figure 4. This is evident even from the grain size measurement shown in Figure 5. Nevertheless, while the grain size continuously decreases in the silica-containing ice, the size increases from 10 to 20% strains in the pure ice. Surprisingly, the sGB densities in both types of ice are almost saturated.

3.3. Dislocation densities in the crept ice

An example of the XRD profile obtained from the as-sintered ice is shown in Figure 6. We assume that the crystal is hexagonal ice (Ih) with the space group symbol of $P6_3/mmc$ (No. 194), with lattice parameters of $a = 0.4501$ nm and $c = 0.7348$ nm: only oxygen sites of $1/3, 2/3, z_0; 1/3, 2/3, 1/2 - z_0; 2/3, 1/3, 1/2 + z_0$ and $2/3, 1/3, 1 - z_0$ are considered (Hobbs, 1974; Petrenko and Whitworth, 1999). The parameter z_0 represents a small shift of the hexagonal rings in the plane normal to the c -axis. z_0 is reported to be 0.0622. Based on this crystal structure the Miller indices are assigned to all the diffracted peaks shown in Figure 6, although they do not usually represent the *four indices* for hexagonal materials. Some small deviations from the ideal Bragg angles for ice Ih indeed appear. We neglect them as they are trivial and measure the modified WH and WA plots from some independent Bragg peaks appearing at more than 20°.

During the calculations we used the hypothesis that the dislocation slips almost occur exclusively based on the basal slip system $\langle 11\bar{2}0 \rangle$ (0001) (Hondoh, 2000), even during the creep deformations under our experimental conditions. Then $\bar{C}_{hk,0}$ parameter in Eq. (10) was calculated using a computer program called ANIZC (Borbély and others, 2003) which provided us with the average dislocation contrast factor by inputting the second order elastic constants C_{ij} or elastic stiffness constants S_{ij} . The values used for $C_{11}, C_{12}, C_{13}, C_{33}$ and C_{44} were 13.20, 6.69, 5.84, 14.42 and 2.89 GPa, respectively, and c/a was 1.63 (Hobbs, 1974). Here, c/a indicates the ratio of the c lattice parameter to the a lattice parameter.

The measured dislocation densities as a function of the strain are summarised in Figure 7. The minimum and maximum dislocation densities obtained in this study range from 10^{11} to 10^{16} m^{-2} . The absolute values are quite high, and some reported dislocation densities for metallic alloys are on the order of 10^{14} m^{-2} using the modified WH and WA methods (Yin and others, 2003; Shintani and Murata, 2011). We must note that the dislocation density reaches 1.4×10^{14} m^{-2} even in the as-sintered pure ice in our case. This may indicate that dislocation densities significantly increase during the pressure-sintering process. Indeed metallic alloys subjected to severe plastic deformation, such as cold-working, show dislocation density greater than 10^{15} m^{-2} (Saymour and others, 2017). Though the same process was used for the fabrication of the silica-containing ice, the density is 3.8×10^{11} m^{-2} . The decrease in the dislocation densities in the silica-containing ice just after

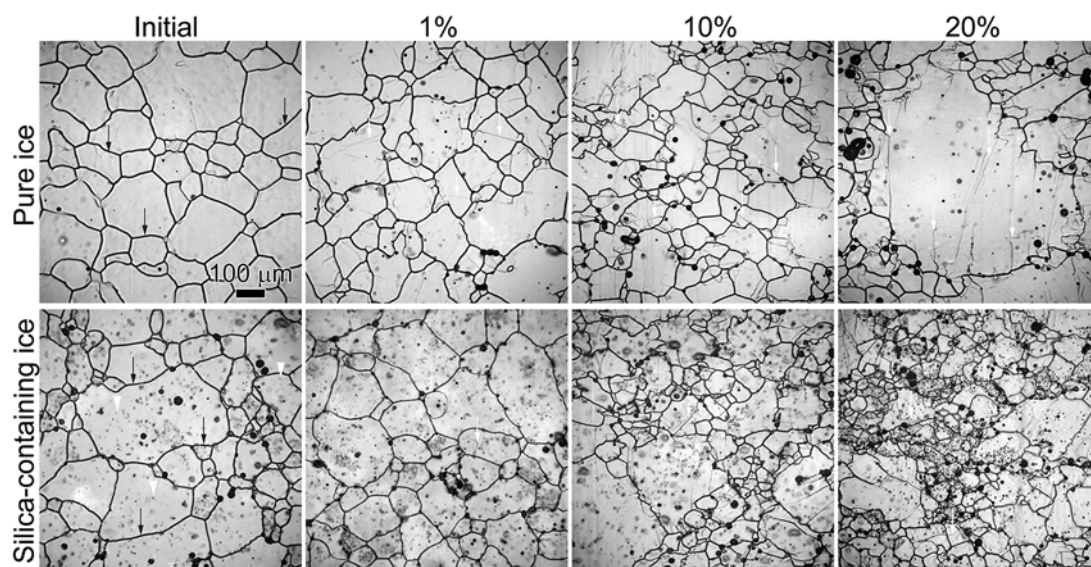


Figure 4. Optical microscope images before and after creep deformations were obtained from pure and silica-containing ice. 'Initial' indicates the initial state before the creep deformations, and 1%, 10% and 20% indicate interrupted creep strains as shown in Figure 3.

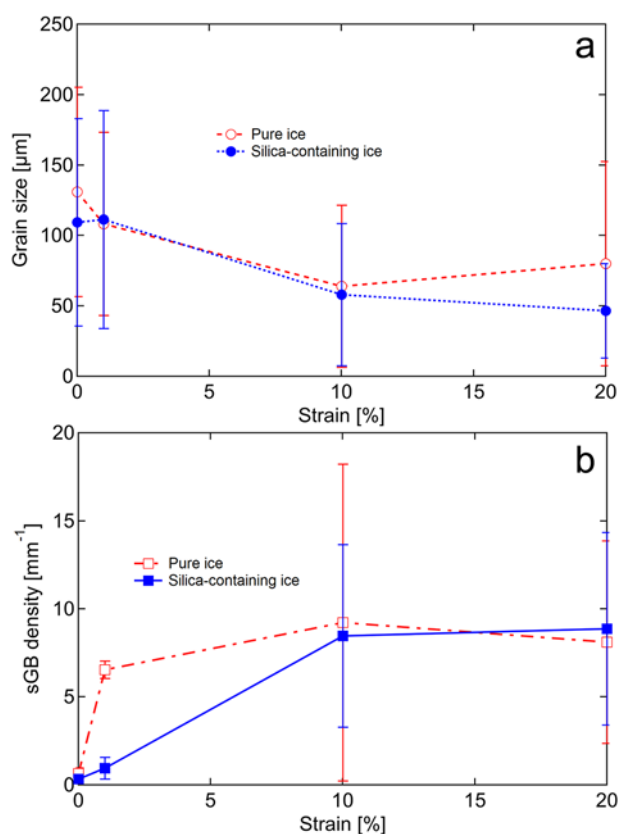


Figure 5. Average grain size or subgrain boundary density as a function of strain measured at -20°C and 2 MPa.

sintering could be explained by the behaviour of creep deformations of the silica-containing ice at 20% strain, as mentioned below. At least we can discuss the relative dependence of the silica addition on the changes of dislocation densities by comparing between pure and silica-containing ice.

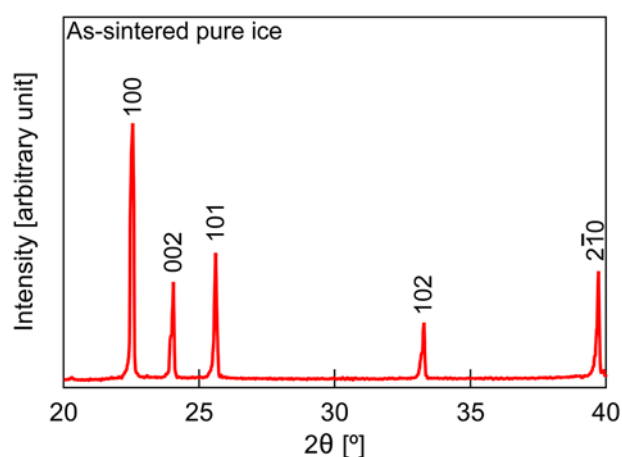


Figure 6. XRD profile obtained from as-sintered pure ice.

At 1% strain dislocation densities in both types of ice rapidly increase. In the silica-containing ice it shows a two orders of magnitude increase compared to the initial state. Nevertheless, although the dislocation densities increase, the grain sizes do not alter. The sGBs rapidly increase in the pure ice, but they do not increase in the silica-containing ice (Figure 5). The strain rate-strain diagrams shown in Figure 3 reveal a rapid decrease in the strain rate in both samples, and the pure ice is harder. Hence, it can be concluded that the rapid decrease in the strain rate is related to work hardening, particularly in the pure ice in the primary creep regime. Similar conclusions are drawn in our previous paper (Saruya and others, 2019); the hardening behaviours of the strain rate-strain diagrams are related to dislocation pile-ups. However the silica-containing ice shows a rapid decrease in the strain rate until the 0.5% strain. Hence dispersion hardening (Ashby and Jones, 1980) may occur only in the initial stage of the deformation, but it does not continue in the later stage of the deformation. The dislocation density at 10% strain slightly decreases or remains almost consistent with that in the 1% strained sample in the pure

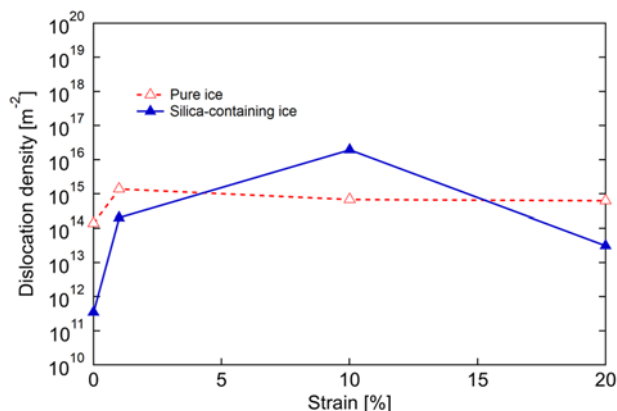


Figure 7. Dislocation densities measured using modified WH and WA plots for pure and silica-containing ice as a function of strain.

ice and work hardening continues, while it exhibits the maximum density in the silica-containing ice. Simultaneously the grain sizes decrease and the sGB densities increase. This means recrystallisation occurs in addition to a sufficient increase of dislocations (Humphreys and Hathery, 2004): it is confirmed in Figure 4. Some dislocations are used for the formation of sGBs (Figure 5) as well as strain hardening; therefore the strain rates decrease compared with those in the initial stage of the creep.

In both types of ice the strain rates continuously decrease as shown in Figure 3. This is also consistent with what we reported previously (Saruya and others, 2019). However, the dislocation densities show different behaviour. Although the measured dislocation densities are almost constant in the pure ice after the 1% strain, the density rapidly decreases in the silica-containing ice at 20% strain. The decrease is more than two orders of magnitude. Figure 5 suggests that the grain size of the silica-containing ice continuously decreases from 10% strain, while in pure ice it remains almost constant within the error bars. The sGB densities do not significantly change with or without the silica addition. The grain refinement must be related to the occurrence of dynamic recrystallisation, which consumes dislocations for the nucleation of new crystalline grains (Humphreys and Hathery, 2004), but at the same time relatively large grains also remain (Figure 4); we can see zig-zag shapes of the GBs, i.e., occurrence of strain-induced boundary migrations (SIBM, Faria and others, 2014). The occurrence of SIBM is also confirmed in the pure ice. Again the hardening effect in the pure ice at 20% strain compared with that of the silica-containing ice (Figure 3) can be explained by work hardening, the occurrences of which is directly confirmed in Figure 7. Thus the silica addition promotes dislocation annihilations near the grain boundaries of the fine grains (Gifkens, 1976) due to the pinning effect of the silica additions, leading to a decrease in the dislocation density at 20% strain. Hence the silica-containing ice is softer than the pure ice (Figure 3).

3.4. Rough calculations of dislocation velocities in the crept ice

Lastly the dislocation velocities in pure and silica-containing ice were roughly calculated based on Eq. (1) by considering only the basal glide during the creep deformation. The velocities were evaluated at the 10% strains. The dislocation velocities in the pure and silica-containing ice are 3.10×10^{-12} and 4.17×10^{-14} m s⁻¹, respectively, assuming that the measured dislocations include both

geometrically necessary dislocations and statistically stored dislocations (Ashby, 1970). It should be emphasised that the dislocation velocity in the silica-containing ice is two orders of magnitude lower than that in the pure ice. The delay in the dislocation velocity could be related to the presence of nanoscale silica particles, which could also be dispersed on the basal planes. At the creep temperature dislocation glide and climb should occur simultaneously. It is difficult to consider uniform distributions of the silica in the ice crystals, but some segregations can easily be expected, as such uniformly dispersed particles are usually unrealistic in the case of composite materials (for example, Homma and others, 2009). This means that dislocations might be pinned at the densely distributed silica regions. Such regions can be seen in the 10% and 20% strained samples shown in Figure 3. The orders of magnitude of the dislocation velocities are smaller than those reported by other researchers, although they are calculated or measured (Perez and others, 1978; Higashi, 1988). The reported minimum velocity was around 10^{-6} to 10^{-9} m s⁻¹ (Forouhi and Bloomer, 1978; Whitworth, 1978) using single crystals and X-ray diffraction topography methods. This indicates that since dislocation densities in the single crystal ice are lower, dislocation tangles in the polycrystalline artificial ice sufficiently reduce the velocities.

In the case of the steady-state creep with a constant-stress condition the steady-state creep rate is expressed as

$$\dot{\epsilon} = B\sigma^m \exp\left(-\frac{Q}{kT}\right) \quad (15)$$

according to Weertman (Weertman, 1973). Here B is a constant, σ the applied stress, Q an activation energy, k Boltzmann's constant and T the absolute temperature. Weertman then estimated:

$$\rho = \left(\frac{\beta\sigma}{\mu b}\right)^2 \quad (16)$$

if the average internal stress generated by dislocation tangles is equivalent to dislocation densities, where β is a constant. The velocity of dislocations is given by

$$v = \gamma\sigma \exp\left(-\frac{Q}{kT}\right) \quad (17)$$

where γ is a constant. Glen identified the stress exponent as 3.7 (1955), which is slightly larger than that reported by Weertman (1973). Based on the equations we understand that the dislocation density is one of the important factors in determining the steady-state creep rate. Using Eq. (17) the constant γ for the pure and silica-containing ice can roughly be determined using activation energies reported by Saruya and others (2019). These are 60 and 66 kJmol⁻¹ for the pure ice and 0.1% silica-containing ice, respectively. By replacing Boltzmann's constant with the gas constant we obtain the γ values in Eq. (17) as 3.8×10^{-6} and 8.8×10^{-7} m Pa⁻¹ s⁻¹ for the pure and silica-containing ice, respectively. These results suggest that the dislocation velocities with microparticles should almost always be lower than those in pure ice at the steady-state creep region in our experimental conditions.

4. Conclusions

The cold stage and sample holder for X-ray diffraction measurements of ice were developed using a nitrogen gas combined with liquid nitrogen. The obtained X-ray diffraction patterns were analysed based on the modified Warren-Averbach (WA) and modified Williamson-Hall (WH) plots of X-ray line broadening; this is

the first report to accomplish dislocation measurements with the modified WH and WA methods for ice samples.

Dislocation densities as a function of strains were measured from the modified WA and WH plots using artificial ice with and without silica. The silica models the existence of impurities in ice sheets. The X-ray diffraction system was set in a room maintained at ambient temperature. The creep tests were conducted at -20°C and 2 MPa.

In the initial ice large amounts of dislocations are stored due to the sintering process, which uses 70 MPa of the sintering pressure. In the primary creep region dislocation densities increase with the increase in the grain size, particularly in pure ice. Since the aggregates of silica act as pinning sites for grain growth, the grain sizes in the silica-containing ice are relatively smaller than those in the pure ice. The maximum dislocation densities are achieved at 10% strain, with high subgrain boundary densities, while at 20% strain, the density decreases. However the dislocation densities in the pure ice remain almost constant values. The silica dispersions act as pinning sites for the suppression of grain growth. Such small grain sizes may introduce sinks for dislocation annihilations.

The small grain size due to the silica dispersions increases dislocation densities because of the pile-up at grain boundaries at 10% strain. The dislocation velocity was roughly calculated based on the Rowan equation. As can easily be estimated, the silica addition retards the dislocation velocity compared with that in pure ice due to the grain refinement and large number of dislocations.

Acknowledgements. We acknowledge all the members of the Arctic Challenge for Sustainability (ArCS). This research was supported by ArCS (program grant number JPMXD1300000000), JSPS KAKENHI (grant numbers JP15K13567, JP17H02957 and JP18H04140), Japan Arctic Research Network Center (J-ARC Net) in 2017 and NIPR through General Collaboration Project, Japan no. 27-16 and 30-13.

We also acknowledge Dr. Morimasa Takata of Nagaoka University of Technology, Japan for his enthusiastic mentorship regarding the research and developments of the instruments for X-ray diffraction measurements and cooling systems at low temperature.

Author contributions. This study was conceptualized by Nobuhiko Azuma and Tomoyuki Homma with guidance from Kumiko Goto-Azuma. Tomoyuki Homma led the experimental and theoretical work, directed experimental plans and co-authored the paper with Kumiko Goto-Azuma and Nobuhiko Azuma. Tomoyuki Homma and Kazuteru Hirai developed the systems for X-ray diffraction measurements, including the cooling systems and conducted the experimental work. Particularly Kazuteru Hirai was responsible for the data analysis. Kumiko Goto-Azuma and Nobuhiko Azuma were supervised, reviewed and edited. All authors contributed to the discussions of the results and drafting of the manuscript.

References

- Ashby MF (1970) The deformation of plastically non-homogeneous materials. *Philosophical Magazine* **21**(170), 399–424. doi: [10.1080/14786437008238426](https://doi.org/10.1080/14786437008238426)
- Ashby MF and Jones DRH (1980) *Engineering Materials*. Oxford: Pergamon Press.
- Azuma N (1994) A flow law for anisotropic ice and its application to ice sheets. *Earth and Planetary Science Letters* **128**(128), 601–614. doi: [10.1016/0012-821X\(94\)90173-2](https://doi.org/10.1016/0012-821X(94)90173-2)
- Azuma N (1995) A flow law for anisotropic polycrystalline ice under uniaxial compressive deformation. *Cold Regions Science and Technology* **23**(2), 137–147. doi: [10.1016/0165-232X\(94\)00011-L](https://doi.org/10.1016/0165-232X(94)00011-L)
- Azuma N and Goto-Azuma K (1996) An anisotropic flow for ice-sheet ice and its implications. *Annals of Glaciology* **23**, 202–208. doi: [10.3189/S0260305500013458](https://doi.org/10.3189/S0260305500013458)
- Azuma N, Miyakoshi T, Yokoyama S and Takata M (2012) Impeding effect of air bubbles on normal grain growth of ice. *Journal of Structural Geology* **42**, 184–193. doi: [10.1016/j.jsg.2012.05.005](https://doi.org/10.1016/j.jsg.2012.05.005)
- Borbély A, Dragomir-Cernatescu J, Ribárik G and Ungár T (2003) Computer program ANIZC for the calculation of diffraction contrast factors of dislocations in elastically anisotropic cubic, hexagonal and trigonal crystals. *Journal of Applied Crystallography* **36**, 160–162. doi: [10.1107/S0021889802021581](https://doi.org/10.1107/S0021889802021581)
- Budd WF and Jacka TH (1989) A review of ice rheology for ice sheet modelling. *Cold Regions Science and Technology* **16**(2), 107–144. doi: [10.1016/0165-232X\(89\)90014-1](https://doi.org/10.1016/0165-232X(89)90014-1)
- Cuffey KM and Paterson WSB (2010) *The Physics of Glaciers*, 4th edn. London: Elsevier.
- Dragomir IC and Ungár T (2002) Contrast factors of dislocations in the hexagonal crystal system. *Journal of Applied Crystallography* **35**(5), 556–564. doi: [10.1107/S0021889802009536](https://doi.org/10.1107/S0021889802009536)
- Duval P (1981) Creep and fabric of polycrystalline ice under shear and compression. *Journal of Glaciology* **27**(95), 129–140. doi: [10.3189/S002214300001128X](https://doi.org/10.3189/S002214300001128X)
- Duval P, Ashby MF and Anderman I (1983) Rate-controlling processes in the creep of polycrystalline ice. *The Journal of Physical Chemistry* **87**(21), 4066–4074. doi: [10.1021/j100244a014](https://doi.org/10.1021/j100244a014)
- Faria SH, Weikusat I and Azuma N (2014) The microstructure of polar ice. Part II: State of the art. *Journal of Structural Geology* **61**, 21–49. doi: [10.1016/j.jsg.2013.11.003](https://doi.org/10.1016/j.jsg.2013.11.003)
- Forouhi AR and Bloomer I (1978) A quantum mechanical approach to the velocity of dislocation in ice. *Physical Status Solidi (B)* **89**(1), 309–312. doi: [10.1002/pssb.2220890139](https://doi.org/10.1002/pssb.2220890139)
- Fukuda A and Higashi A (1969) X-ray diffraction topographic studies of dislocations in natural large ice single crystals. *Japanese Journal of Applied Physics* **8**(8), 993–999. doi: [10.1143/JJAP.8.993](https://doi.org/10.1143/JJAP.8.993)
- Gifkens RC (1976) Grain-boundary sliding and its accommodation during creep and superplasticity. *Metallurgical Transactions A* **7A**, 1225–1232. doi: [10.1007/BF02656607](https://doi.org/10.1007/BF02656607)
- Glen JW (1952) Experiments on the deformation of ice. *Journal of Glaciology* **2**(12), 111–114. doi: [10.3189/S0022143000034067](https://doi.org/10.3189/S0022143000034067)
- Glen JW (1955) The creep of polycrystalline ice. *Proceedings of the Royal Society of London, Series A* **228**(1175), 519–538. doi: [10.1098/rspa.1955.0066](https://doi.org/10.1098/rspa.1955.0066)
- Groma I, Ungár T and Wilkens M (1988) Asymmetric X-ray line broadening of plastically deformed crystals. I. Theory. *Journal of Applied Crystallography* **21**, 47–53. doi: [10.1107/S0021889887009178](https://doi.org/10.1107/S0021889887009178)
- Hayes CE and Webb WW (1965) Dislocations in ice. *Science* **147**(3653), 44–45. doi: [10.1126/science.147.3653.44](https://doi.org/10.1126/science.147.3653.44)
- Higashi A (ed.) (1988) *Lattice Defects in Ice Crystals*. Sapporo: Hokkaido Univ. Press.
- Hirth JP and Lothe J (1968) *Theory of Dislocations*. New York: McGraw-Hill.
- Hobbs PV (1974) *Ice Physics*. New York: Oxford University Press.
- Homma T, Nagai K, Katou A, Arai K, Suganuma M and Kamado S (2009) Synthesis of high-strength magnesium alloy composites reinforced with Si-coated carbon nanofibers. *Scripta Materialia* **60**(6), 451–454. doi: [10.1016/j.scriptamat.2008.11.024](https://doi.org/10.1016/j.scriptamat.2008.11.024)
- Hondoh T (2000) Nature and behavior of dislocations in ice. In Hondoh T (ed.), *Physics of Ice Core Records*. Sapporo: Hokkaido University Press, 3–24.
- Hooke RL, Dahlin BB and Kauper MT (1972) Creep of ice containing dispersed fine sand. *Journal of Glaciology* **11**(63), 327–336. doi: [10.3189/S0022143000022309](https://doi.org/10.3189/S0022143000022309)
- Hori A, Hondoh T, Oguro M and Lipenkov VY (2004) Ice-lattice distortion along deepest section of the Vostok core from X-ray diffraction measurements. *Annals of Glaciology* **39**, 501–504. doi: [10.3189/172756404781814528](https://doi.org/10.3189/172756404781814528)
- Humphreys FJ and Hathery M (2004) *Recrystallization and Related Annealing Phenomena*, 2nd edn. Amsterdam: Elsevier.
- IPCC (2019) Summary for Policymakers. In Pörtner H-O, Roberts DC, Masson-Delmotte V, Zhai P, Tignor M, Poloczanska E, Mintenbeck K, Alegriam A, Nicolai M, Okem A, Petzold J, Rama B and Weyer NM (eds), *IPCC Special Report on the Ocean and Cryosphere in a Changing Climate*. Cambridge and New York, NY: Cambridge University Press, 3–35.

- Klimanek P and Kužel R, Jr** (1988) X-ray diffraction line broadening due to dislocation in non-cubic materials. I. General considerations and the case of elastic isotropy applied to hexagonal crystals. *Journal of Applied Crystallography* **21**, 59–66. doi: [10.1107/S0021889887009580](https://doi.org/10.1107/S0021889887009580)
- Krivoglaz MA** (1969) *Theory of X-ray and Thermal Neutron Scattering by Real Crystals*. New York: Plenum.
- Lang AR** (1959) Studies of individual dislocations in crystals by X-ray diffraction microradiography. *Journal of Applied Physics* **30**, 1748–1755. doi: [10.1063/1.1735048](https://doi.org/10.1063/1.1735048)
- Muguruma J** (1961) Electron microscope study of etched ice surface. *Journal of Electronmicroscopy* **10**(4), 246–250. doi: [10.1093/oxfordjournals.jmicro.a049315](https://doi.org/10.1093/oxfordjournals.jmicro.a049315)
- Nakaya U** (1956) Properties of single crystals of ice, revealed by internal melting. *Research paper 13*, U.S. Army Snow Ice and Permafrost Research Establishment, Wilmette, Illinois, 1–80(pl. 1–105).
- Nayar HS, Lenel FV and Ansell GS** (1971) Creep of dispersions of ultra-fine amorphous silica in ice. *Journal of Applied Physics* **42**, 3786–3789. doi: [10.1063/1.1659686](https://doi.org/10.1063/1.1659686)
- Perez J, Mai C and Vassoille R** (1978) Cooperative movement of H₂O molecules and dynamic behaviour of dislocations in ice Ih. *Journal of Glaciology* **21**(85), 361–374. doi: [10.3189/S0022143000033530](https://doi.org/10.3189/S0022143000033530)
- Petrenko VF and Whitworth RW** (1999) *Physics of Ice*. New York: Oxford University Press, 0–19–851894–3.
- Poirier JP** (1976) *Plasticité a Haute Temperature Des Solides Cristallins*. Paris: Eyrolles.
- Saruya T, Nakajima K, Takata M, Homma T, Azuma N and Goto-Azuma K** (2019) Effects of microparticles on deformation and microstructural evolution of fine-grained ice. *Journal of Glaciology* **565**(252), 531–541. doi: [10.1017/jog.2019.29](https://doi.org/10.1017/jog.2019.29)
- Saymour T and others** (2017) Evolution of dislocation structure in neutron irradiated Zircaloy-2 studied by synchrotron x-ray diffraction peak profile analysis. *Acta Materialia* **126**, 102–113. doi: [10.1016/j.actamat.2016.12.031](https://doi.org/10.1016/j.actamat.2016.12.031)
- Shintani T and Murata Y** (2011) Evaluation of the dislocation density and dislocation character in cold rolled Type 304 steel determined by profile analysis of X-ray diffraction. *Acta Materialia* **59**(11), 4314–4322. doi: [10.1016/j.actamat.2011.03.055](https://doi.org/10.1016/j.actamat.2011.03.055)
- Song M, Baker I and Cole DM** (2008) The effect of particles on creep rate and microstructures of granular ice. *Journal of Glaciology* **54**(186), 533–537. doi: [10.3189/002214308785836959](https://doi.org/10.3189/002214308785836959)
- Song M, Cole DM and Baker I** (2004) Initial experiments on the effects of particles at grain boundaries on the anelasticity and creep behavior of granular ice. *Annals of Glaciology* **39**, 397–401. doi: [10.3189/172756404781814069](https://doi.org/10.3189/172756404781814069)
- Ungár T, Gubicza J, Ribárik G and Borbély A** (2001) Crystallite size distribution and dislocation structure determined by diffraction profile analysis: Principles and practical application to cubic and hexagonal crystals. *Journal of Applied Crystallography* **34**(3), 298–310. doi: [10.1107/S0021889801003715](https://doi.org/10.1107/S0021889801003715)
- Ungár T, Ott S, Sanders PG, Borbély A and Weertman JR** (1998) Dislocation, grain size and planar faults in nanostructured copper determined by high resolution X-ray diffraction and a new procedure of peak profile analysis. *Acta Materialia* **46**(10), 3693–3699. doi: [10.1016/S1359-6454\(98\)00001-9](https://doi.org/10.1016/S1359-6454(98)00001-9)
- Warren BE and Averbach BL** (1950) The effect of cold-work distortion on X-ray patterns. *Journal of Applied Physics* **21**(6), 595–599. doi: [10.1063/1.1699713](https://doi.org/10.1063/1.1699713)
- Warren BE and Averbach BL** (1952) The separation of cold-work distortion and particle size broadening in X-ray patterns. *Journal of Applied Physics* **23**(4), 497–497. doi: [10.1063/1.1702234](https://doi.org/10.1063/1.1702234)
- Weertman J** (1973) Creep of ice. In Whalley SJ, Jones SJ and Gold LW (eds), *Physics and Chemistry of Ice*. Can., Ottawa: R. Soc, 320–337.
- Whitworth RW** (1978) The core structure and the mobility of dislocations in ice. *Journal of Glaciology* **85**(85), 341–359. doi: [10.3189/S0022143000033529](https://doi.org/10.3189/S0022143000033529)
- Wilkens M** (1967) Das Spannungsfeld einer Anordnung von regellos verteilten Versetzungen. *Acta Metallurgica* **15**(8), 1412–1415. doi: [10.1016/0001-6160\(67\)90020-X](https://doi.org/10.1016/0001-6160(67)90020-X)
- Wilkens M** (1969) Theoretical aspects of kinematical X-ray diffraction profiles from crystals containing dislocation distributions. In Simmons JA, de Wit R and Bullough R (eds), *Conference Proceedings of Fundamental Aspects of Dislocation Theory*, Washington: National Bureau of Standards, 1195–1221.
- Williamson GK and Hall WH** (1953) X-ray line broadening from field aluminum and wolfram. *Acta Metallurgica* **1**(1), 22–31. doi: [10.1016/0001-6160\(53\)90006-6](https://doi.org/10.1016/0001-6160(53)90006-6)
- Yin F, Hanamura T, Umezawa O and Nagai K** (2003) Phosphorus-induced dislocation structure variation in the warm-rolled ultrafine-grained low-carbon steels. *Materials Science and Engineering: A* **354**(1-2), 31–39. doi: [10.1016/S0921-5093\(02\)00766-9](https://doi.org/10.1016/S0921-5093(02)00766-9)